International Journal on Magnetic Particle Imaging
Vol 4, No 1, Article ID 1809001, 5 Pages

Infinite Science Publishing

Research Article

Design of a Permanent Magnet Selection Field Structure for a Single-Sided Field-Free Line Magnetic Particle Imaging Scanner

Grant Rudd[a] · Alexey Tonyushkin[b,*]

[a]Engineering Department, University of Massachusetts Boston, Boston, MA 02125 USA
[b]Physics Department, University of Massachusetts Boston, Boston, MA 02125 USA
*Corresponding author, email: alexey.tonyushkin@umb.edu

Received 17 March 2018; Accepted 03 July 2018; Published online 12 September 2018

Abstract

The single-sided scanner configuration is one of the most recent developments in the field of magnetic particle imaging (MPI). The main difference between the single-sided and the conventional symmetric configurations is in the co-planar topology of the selection coils in the former type. Although it is challenging to create high-strength gradients with a uniform field in the single-sided configuration, such a device provides the benefit of imaging of the near-surface regions of large objects that cannot be accommodated by the symmetric configuration. Current state-of-the-art single-sided scanners utilize a field-free point (FFP) selection field. Previously, we presented a concept of a single-sided device based on a field-free line (FFL) with permanent magnets (PM). Here, we report on the progress of the development of a single-sided field-free line MPI scanner with PM selection field structure, which is capable of producing a strong field gradient of G=3 T/m at a height of 3 cm above the surface. Implementation of the PM structure as a selection field generator is especially valuable in an FFL scanner since it alleviates some technical issues of power managements in a rotating setup.

I. Introduction

Over the last decade, magnetic particle imaging (MPI) [1] has evolved into a new imaging modality that holds promise for a variety of clinical applications [2]. One of the recent MPI developments is a single-sided MPI scanner based on a field-free point (FFP) [3–5]. In the single-sided scanner, all the hardware is located on one side from the imaging volume, therefore it can alleviate spatial constraints particularly pertinent to the imaging of large subjects. Although such a scanner has a relatively shallow field of view, it could be a solution for a number of clinical applications [6, 7].

Previously, we presented the concepts of the single-sided devices based on a field-free line (FFL) with permanent magnet (PM) [8] and electromagnetic [9] selection field structures. In this work, we present the demonstrator of the PM structure that will be utilized in a single-sided scanner to create static selection field.

II. Material and Methods

II.I. Magnet design

The PM assembly is shown in Figure 1. The parts of the PM enclosure were prototyped on a 3D printer (Markforged Mark 2) out of carbon fiber-reinforced nylon. The enclosure is assembled out of six identical elements

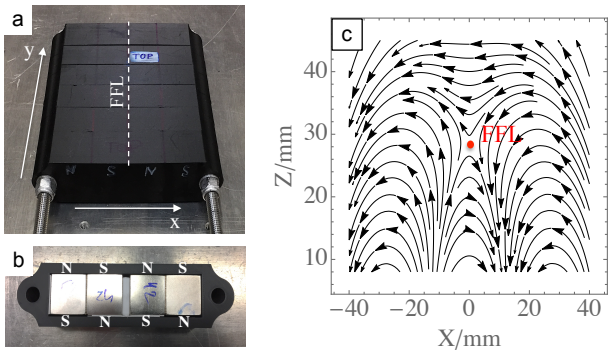

Figure 1: Permanent magnet selection field assembly. The assembly (a) consists of six identical elements (b) with four alternating-pole magnets in each element. FFL is obtained above the surface in the isoplane (dashed line); vector plot of the magnetic flux density in the xz-plane (c) showing the FFL (red dot) at $z_0 \approx 3$ cm.

Table 1: Properties of NdFeB cube magnets.

PM grade	N38	**N42**	N48	**N52**
$B_{\mathrm{rmax}}[T]$	1.26	1.32	1.38	1.48
$M[T/\mu_0]$	0.549	0.575	0.601	0.645

(rows along x-axis) with a total assembly size of 16.5 cm x 15.5 cm, as shown in Figure 1. Each row consists of four tightly packed 2.54 cm-cube NdFeB magnets with a 0.5 cm spacer in the middle. The magnets are arranged in a row with the alternating poles pointing at the surface of the structure (Figure 1(b)) that forms the basis for the static selection field (Figure 1(c)) [8]. Each element consists of two different grades of NdFeB magnets: N52 and N42 - the outer and the inner pairs of magnets, respectively.

The residual induction B_{rmax} and surface magnetization M of different PM grades in a cube configuration are given in Table 1. The specifications in the table provide the magnetization ratio $m = M_2/M_1$, which is the main parameter for predicting the properties of the selection field, such as the height of the FFL [8]. In principle, to achieve the maximum possible strength of the magnetic field gradient and, thus highest spatial resolution, such PM structure has to be composed of the two highest available grades N48 and N52. For this demonstrator, due to the commercial availability of the cubes in a wide variety of shapes and sizes we chose N42 and N52 with $m = 1.12$, which give us a balanced choice of high field gradient and fairly large static depth. For the chosen grades, the selection field properties are defined by the size of the building cubes. One of the main requirements of the selection field structure is the compactness since it affects the design and the power requirement of the surrounding electromagnetic coils. However, small size of PM structure may contradict with the requirements

Table 2: Selection field versus PM cube size.

Cube size [cm]	1.27	2.54	3.81	5.08	7.62
$G_{\mathrm{max}}[T/m]$	7.4	4.2	2.6	2	1.3
h(FFL) [cm]	1.28	2.56	3.82	5.1	7.7

on the field uniformity and linearity of the gradient.

The comparison of the maximum magnetic field gradient G_{max} and the height of the FFL h in the optimal tightly packed four-element configuration of cubes of various sizes composed of two grades (N52 and N42), is shown in Table 2. In this work, we describe the demonstrator PM structure made of 2.54 cm cubes that achieves a uniform field, while been compact enough to incorporate drive coils. Since the optimal configuration from the high-gradient point of view has a limited static FFL height, it may affect the final design of the scanner and limit its application. Therefore, a spacer can be added to increase the static height of the FFL to the projected one, though at the expense of a reduced gradient of the magnetic field.

Another feature that is highly desired in the FFL-based MPI scanners is the linearity of the field along the FFL direction. A single-sided FFL scanner has a finite curvature associated with the FFL [9]. To decrease the curvature of the generated FFL, we utilize six magnets along the FFL bringing the total length to $L = 15.24$ cm. To characterize the magnetic flux density **B** of the PM coils, we carried out simulations and measurements

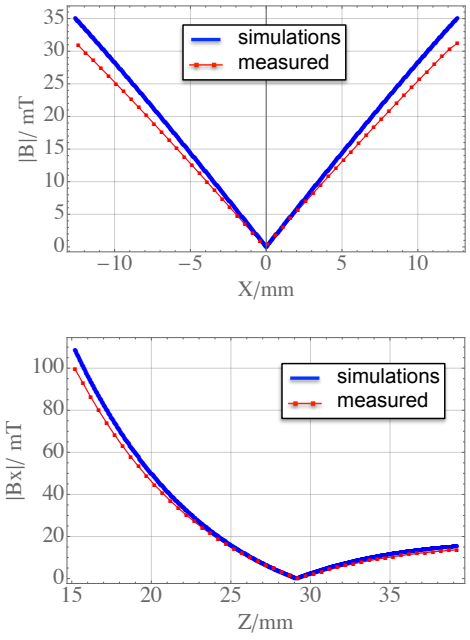

Figure 2: Simulations (solid line) and measurements (dot-solid line) of the magnetic flux density from the PM, top: |B| along x-axis ($z_0 = 2.9$ cm), bottom: $|B_x|$ along z-axis ($x_0 = 0$).

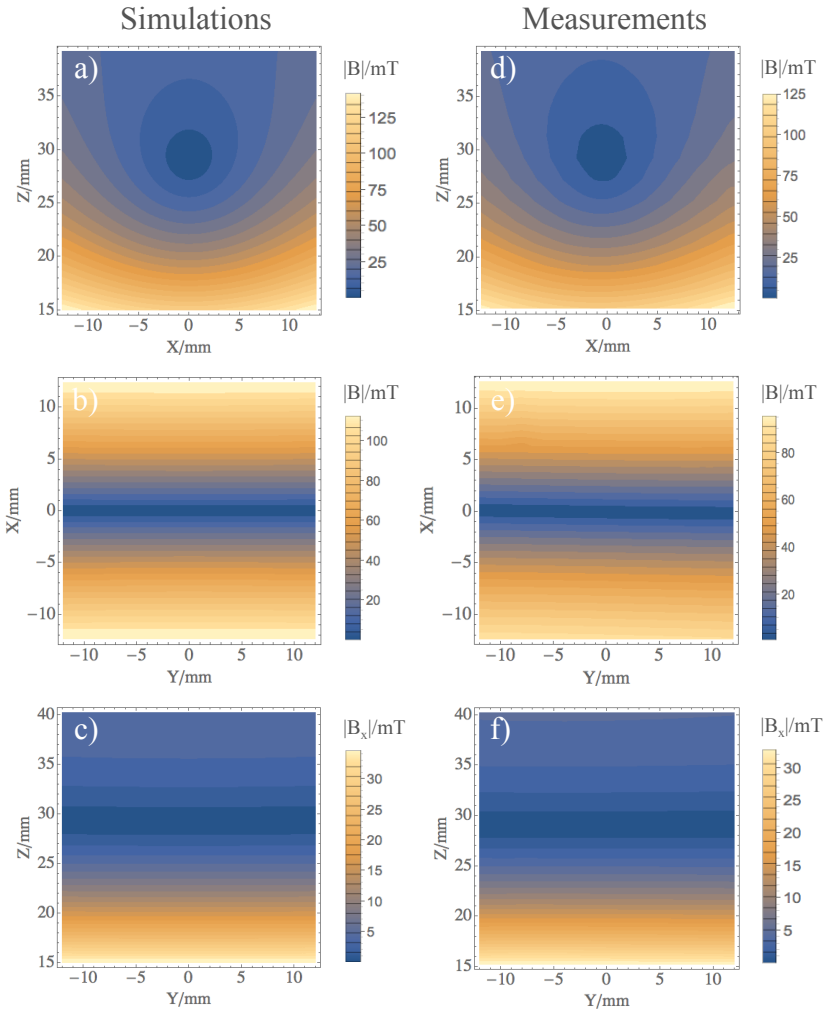

Figure 3: Simulations (a)-(c) and measurements (d)-(f) of the magnetic flux density |B| from the PM coils: (a),(d) *xz*-plane; (b),(e) *yx*-plane; (c),(f) *yz*-plane.

using boundary Integral Methods of Radia package [10] interfaced with Mathematica (Wolfram) and a gaussmeter (Magsys) with a single-axis hall probe. The probe was mounted on micrometer-precision translation stages and scanned across different planes within the volume of interest, while recording each Cartesian component of the magnetic flux density. The total flux density $|B|$ is calculated after obtaining all the components of the field.

III. Results

III.I. Simulations and measurements

The designed PM structure generates an FFL at the static height of $h = 2.90 \pm 0.05$ cm above the surface of the magnets, which includes the 0.635 cm thickness of the enclosure. Figure 1(c) shows a simulated vector plot of the magnetic flux density in the *xz*-plane. A characteristic property of the PM arrangement is that, at the isoplane $x = 0$, $B_z = 0$.

The plots of the simulated and measured magnetic flux densities |B| along *x*- and *z*- axes are shown in Figure 2. The calculated and measured field gradients are $G = 3.25$ T/m and $G = 2.91$ T/m, respectively. The 10% difference between the simulated and the measured gradients is attributed to a non-uniform distribution of the magnetization on the surface, which corresponds to a lower effective magnetization of the PM cube than the specified one. This discrepancy does not affect the magnetization ratio m; thus the height h is unchanged.

The corresponding 2D plots of |B| generated by the PM are shown in Figure 3: the top row shows cross-sections of the FFL in the *xz*-plane; the middle and bottom rows show the curvatures of the FFL in the *xy*- and *zy*- planes, respectively. Apart from the 10% difference in magnitude the simulations and the measurements of the magnetic field match each other. The quality of the FFL

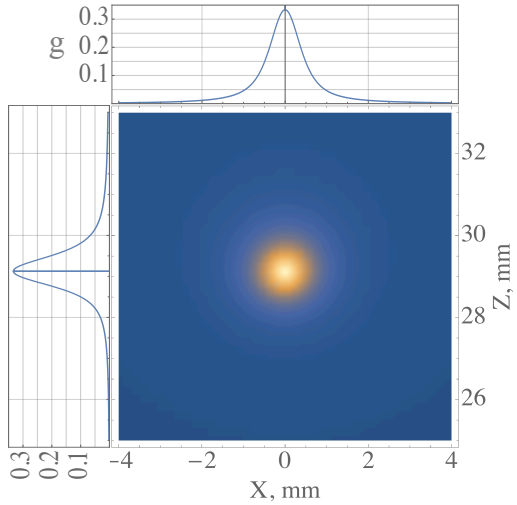

Figure 4: Simulated PSF of PM structure with the respective projections on the x- and z-axes that give estimates for the spatial resolutions.

is represented by the linearity of the magnetic field in the xy- and zy- planes (Figure 3(b)(e) and (c)(f), respectively). Both the simulations and the measurements show good linearity of the FFL over a region of 2 cm. The calculated curvature of the FFL along the y-axis is 320 μT/cm^2, which is sufficiently small to provide a few-cm encoding region; adding more elements to the assembly would further decrease the curvature.

To characterize the spatial resolution of PM structure, we calculated the point-spread function (PSF) of the simulated static selection field $H_s(x,z)$ according to $g(x,z) = L'(\xi)$ for $\xi = \mu_0 M_0 \pi D^3 H_s(x,z)/(6k_B T)$, where $L(\xi)$ is the Langevin function that describes the magnetization response of the superparamagnetic iron oxide (SPIO) nanoparticles, $M_0 = 0.6T/\mu_0$ is the saturation magnetization of the SPIO, D is the magnetic core diameter, T is temperature, μ_0 is the vacuum permeability, and k_B is Boltzmann's constant. The simulated 2D PSF of the PM structure is shown in Figure 4. For an idealized SPIO with $D = 30$ nm at T=25^{0}C it yields a spatial resolution of 1 mm.

IV. Discussion and Outlook

The described PM selection structure produces a strong field gradient that is desired for an imaging with high spatial resolution. Depending on the application, the static height of the FFL, which defines the encoding slice, can be changed by varying the gaps between the pairs of magnets in each row, or increasing the size of the magnets. For example, increasing the separation of the outer pairs by 2 cm would move the height up to 3.6 cm, while decreasing the field gradient to 2.1 T/m.

Multidimensional imaging may be realized in a scanner design, as proposed in [8]. In a future work, a modified arrangement for such a scanner will combine the presented PM assembly with the elongated electromagnetic coils. A proposed setup of the single-sided scanner is shown in Figure 5. In such a concept design, the PM structure replaces the DC electromagnets, while the two sets of drive coils on top and on the bottom provide oscillation and focusing of the FFL, respectively. To prevent induced eddy current from the top coils and thus heating of the PM, there is an additional copper shield required between the PM and the top set of coils. The complete setup will be mounted on a gantry that can rotate around the z-axis for 0-180^0, allowing in-plane projection image reconstruction [11].

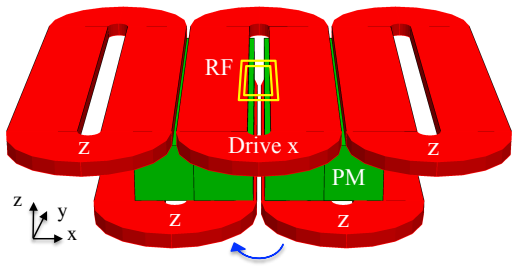

Figure 5: A concept of the FFL single-sided scanner with PM. Here, RF - radiofrequency coil, PM - permanent magnets; x, z are corresponding directions of the drive coils.

Two imaging approaches can be realized with the above setup. In the first approach, the x- and z-drive coils on top (Figure 5) would allow encoding a Lissajous pattern in xz-plane thus implementing imaging with a system function method. Alternatively, for xy-plane imaging, only a single x-drive coil placed along the isoaxis and a corresponding single receive channel are needed. Such a coil provides oscillations ($f \approx 20$ kHz) of the FFL along the x-axis. A mechanical or electronic slice selection with a pair of z-drive coils on the bottom provide focusing of the field with the frequency of ~ 10 Hz. This approach can be utilized in x-space imaging [12].

For the typical drive coils [9], the estimated span of the FFL in such a device is ~ 2 cm along x-axis and ~ 1 cm along z-axis for the maximum peak current of up to 100 A. At the same time the gradient G will change from 5 T/m to 1.1 T/m from the lowest to the highest translation points along the z-axis, respectively. Correspondingly, that variation yields a range of spatial resolutions along z-axis of 0.6 mm to 3 mm if gradient is left uncompensated. A gradient correction algorithm can be applied to z-drive coils as described in [9].

The detection of an MPI signal in a single-sided FFL scanner requires a spatially selective surface radiofrequency (RF) loop coil. The polarization of the field from the receive coils has to match the polarization of the corresponding drive field, so a loop coil placed at the center of the PM coils, as shown in Figure 5, matches

10.18416/ijmpi.2018.1809001

the direction of the field produced by the x-drive coil. The geometry of the RF coil defines its spatial selection profile, which has to overlap with the linear region of the FFL. In two-channel version, oscillations along the z-axis can be detected by a surface "figure-8" loop receive coil, which matches the direction of the field produced by the z-drive coils.

V. Conclusions

We designed and tested permanent magnet selection field demonstrator for a single-sided FFL-based MPI scanner. The demonstrator generates a static FFL 3 cm above the surface, with a field gradient of $G = 3$ T/m. In combination with mechanical rotation and translation by the AC coils, such an MPI device can provide a strong magnetic field gradient with a sufficient field of view at reduced power consumption. This demonstrator will be incorporated into a new FFL-based single-sided MPI scanner.

Acknowledgment

We acknowledge support from the University of Massachusetts President's Office through an OTCV Award.

References

[1] B. Gleich and J. Weizenecker. Tomographic imaging using the nonlinear response of magnetic particles. *Nature*, 435(7046):1214–1217, 2005, doi:10.1038/nature03808.

[2] T. Knopp and T. M. Buzug, Magnetic Particle Imaging: An Introduction to Imaging Principles and Scanner Instrumentation. Berlin, Heidelberg: Springer Berlin Heidelberg, 2012, doi:10.1007/978-3-642-04199-0.

[3] T. F. Sattel, T. Knopp, S. Biederer, B. Gleich, J. Weizenecker, J. Borgert, and T. M. Buzug. Single-sided device for magnetic particle imaging. *Journal of Physics D: Applied Physics*, 42(2):022001, 2009, doi:10.1088/0022-3727/42/2/022001.

[4] K. Gräfe, A. von Gladiss, G. Bringout, M. Ahlborg, and T. M. Buzug. 2D Images Recorded With a Single-Sided Magnetic Particle Imaging Scanner. *IEEE Transactions on Medical Imaging*, 35(4):1056–1065, 2016, doi:10.1109/TMI.2015.2507187.

[5] K. Gräfe, A. von Gladiss, and T. M. Buzug, First Phantom Measurements with a 3D Single Sided MPI Scanner, in *International Workshop on Magnetic Particle Imaging*, 2018.

[6] C. Kaethner, M. Ahlborg, K. Gräfe, G. Bringout, T. F. Sattel, and T. M. Buzug. Asymmetric Scanner Design for Interventional Scenarios in Magnetic Particle Imaging. *IEEE Transactions on Magnetics*, 51(2):1–4, 2015, doi:10.1109/TMAG.2014.2337931.

[7] K. Gräfe, T. F. Sattel, K. Lüdtke-Buzug, D. Finas, J. Borgert, and T. M. Buzug, Magnetic-Particle-Imaging for Sentinel Lymph Node Biopsy in Breast Cancer, in *Magnetic Particle Imaging*, 2012, 237–241. doi:10.1007/978-3-642-24133-8_38.

[8] A. Tonyushkin. Single-sided hybrid selection coils for field-free line magnetic particle imaging. *International Journal on Magnetic Particle Imaging*, 3(1), 2017, doi:10.18416/ijmpi.2017.1703009.

[9] A. Tonyushkin. Single-Sided Field-Free Line Generator Magnet for Multi-Dimensional Magnetic Particle Imaging. *IEEE Transactions on Magnetics*, 53(9):1–6, 2017, doi:10.1109/TMAG.2017.2718485.

[10] O. Chubar, P. Elleaume, and J. Chavanne. A three-dimensional magnetostatics computer code for insertion devices. *Journal of Synchrotron Radiation*, 5(3):481–484, 1998, doi:10.1107/S0909049597013502.

[11] J. J. Konkle, P. W. Goodwill, O. M. Carrasco-Zevallos, and S. M. Conolly. Projection Reconstruction Magnetic Particle Imaging. *IEEE Transactions on Medical Imaging*, 32(2):338–347, 2013, doi:10.1109/TMI.2012.2227121.

[12] P. W. Goodwill, J. J. Konkle, Bo Zheng, E. U. Saritas, and S. T. Conolly. Projection X-Space Magnetic Particle Imaging. *IEEE Transactions on Medical Imaging*, 31(5):1076–1085, 2012, doi:10.1109/TMI.2012.2185247.

